



Non-coupled Finite Element Modelling of Electromagnetic Radial Compaction of Pure Aluminium Powder

Nadimetla Thirupathi¹ · Ramesh Kumar² · Sachin D. Kore¹

Received: 20 February 2022 / Revised: 1 October 2022 / Accepted: 15 November 2022 / Published online: 6 January 2023
© The Author(s), under exclusive licence to Korean Society for Precision Engineering 2023

Abstract

In this article, Finite element modelling is described to simulate aluminium powder's electromagnetic radial powder compaction process. Electromagnetic powder compaction technique is considered a high strain and high-speed powder forming technique in which solenoid coil with uniformly tapered step field shaper is used as forming tool for powder compaction process. In this process, the packing tube that holds the powder acts as a driving medium for the momentum transfer. During experiments, aluminium powder is kept in an electrically conductive driver tube material (in this study, Al 6063 tube). This process utilizes the Lorentz forces for compacting powder to give the required strength for the powder metallurgy component. This paper mainly develops a non-coupled finite element model to simulate the aluminium powder's electromagnetic powder compaction process. A versatile software Ansys Maxwell was used to analyze the intensities of the distribution of the electromagnetic fields during the electromagnetic forming process. The current curve obtained in the experiment is used as input loading conditions for analyzing electromagnetic fields. After that, for structural analysis of the powder compaction process, Ls-Dyna explicit software is used. The Geologic cap model was established in Ls-Dyna Multiphysics software for modelling powder deformation behaviour. The Johnson-Cook strength model was used to describe the packing tube's deformation. The FEM analysis helped predict the results of the final shape and size of electromagnetic powder compaction. The developed simulation model has been validated with a series of experiments resulting from the compaction of aluminium powder.

Keywords Electromagnetic radial compaction · Non-coupled finite element modelling · Powder compaction · Numerical modelling

1 Introduction

The electromagnetic powder compaction technique is considered a high-energy rate dynamic compaction technique. It is a very effective method over conventional compaction methods. The concise duration of the compaction and development of the high pressures leads to substantial reductions in the porosity of the powder metallurgy components. In Electromagnetic powder compaction, an action occurs similar to many electromagnetic forming processes such as welding, compression/expansion, and crimping. The controlling and valuable parameters for forming the material

are Lorentz forces in all these processes. So, the powder is compacted by using these Lorentz forces. This process can be treated as a contactless powder compaction technique since no tool comes in contact with powder for forming. This process can compact various materials irrespective of the hardness and size of the powder particle. Few materials are very difficult to compress due to their higher hardness. The frictional forces are very high during the compaction of nano-size metallic powder. These barriers can be easily overcome using high velocity and high energy rate forming techniques such as electromagnetic forming [1].

The electromagnetic powder compaction methods are well suited for compacting nanopowder which is difficult to compact due to its strong interparticle frictions. Hence, nanopowder compaction needs very high pressures in the order of several GPa [2]. Yan et al. studied the electromagnetic powder compaction of Ag-Cu-Sn multi-component powders for solder applications [3]. They have used Ls-Dyna discrete element method to simulate the powder compaction

✉ Ramesh Kumar
remsiitg@gmail.com

¹ Indian Institute of Technology-Goa, Ponda 403401, India

² Saharsa College of Engineering, Saharsa, Bihar 852201, India

phenomena. The powder material was assigned the Johnson-Cook strength model to describe its deformation behaviour during electromagnetic compaction.

Mamalis et al. [4] used the Drucker Prager Cap (DPC) model for FEM analysis of Y-Ba-Cu-O superconducting powder compaction in the explosive compaction method. They validated the simulation results with experiments using the final dimensions of the compacted sample. They also predicted the powder compact's pressure, temperature, and density distribution. Han et al. [5] used a modified density-dependent DPC model for describing the pharmaceutical powder behaviour. User subroutine USDFLD code was implemented in Abaqus standard explicit software to analyze the density variation and stress distribution.

Selig et al. [6] developed Ls-Dyna hydrocode to perform Alumix 321 powder compaction and spring back simulation. Experimental results from optical densitometry analysis agreed with the simulation results. The spring back behaviour of the powder compact after ejection was also analyzed, and results were found to be deviating considerably above 500 MPa compaction pressures. Akhmetshin et al. [7] have used Drucker Prager Cap constitutive model to simulate W-C/Co powders. They analyzed the bulk plastic deformation and stress distribution in hard metal powder. In the numerical simulation of the powder compaction, the powder is considered continuously compressible, which undergoes large elastic-plastic deformation. Cam-Clay, Drucker-Cap and Geologic-Cap models are widely used continuum mechanical models for simulating the powder compaction process [8].

Several high-velocity compaction (HVC) techniques, such as explosive compaction and drop hammer, and various researchers studied hydraulics to obtain high-density and strength compacts through the powder metallurgy process. Pressure shock waves that travel through the powder are used to carry out the HVC procedure. Microscale manufacturing of Al powder metallurgy parts investing by Ni et al. [9] using laser shock dynamic compaction method. 2D multi-particle finite element method (MPFEM) was used to predict how the generated shock wave propagated through powder. Cold welding between particles was observed in the dynamic compaction process. Babaei et al. [10] studied the drop hammer dynamic compaction technique to compact the aluminium powder. The highest density was 95.11%, corresponding to 3.58 kJ potential energy. The mechanical and electrical properties were improved with particle size reduction [11]. The effect of the size of Al powder under high-pressure compaction was investigated by Kim [12].

This paper has validated a series of experimental results using a loosely coupled finite element analysis—aluminium powder used as raw material for electromagnetic radial powder compaction technique. Ansys Maxwell software was used to establish an electromagnetic field model of

electromagnetic radial compaction of aluminium powder. Magnetic field intensity was obtained for various input current loads using Maxwell simulation. The effect of field shaper on the magnetic field and magnetic field distribution at the various location were analyzed using Ansys Maxwell simulation. Then, Ls-Dyna explicit dynamics is used to create a structural field model. The input loading for Ls-Dyna structural analysis was taken from Ansys Maxwell magnetic field results. In this paper, for structural analysis of the powder compaction process, GEO-LOGIC-CAP constitutive model and the Johnson-Cook strength models were used to reproduce the behaviour of powder and packing tube, respectively. Ls-Dyna Explicit was used to predict the final deformation of the powder compacted body, stress distribution within the compact and resultant velocity of the packing tube.

2 Electromagnetic Radial Powder Compaction Theory

The governing principle of the electromagnetic radial powder compaction is described in Fig. 1. The powder-filled conductive metal tube (Al 6063) is placed co-axially inside the field shaper and solenoid coil forming tool. The two terminals of the solenoid coil are connected to the capacitor bank via a triggering switch, and in this way, it forms an RLC circuit. The capacitor bank is charged to the required set voltage (V_0). When the triggering switch is closed, the circuit closes, and the sinusoidal damped current, $I(t)$ with angular frequency (ω_d), gets discharged through the coil. The current flowing in the coil alternatively generates a transient magnetic field about the coil. Since the created magnetic field is time-dependent and sine wave, it induces an eddy current in the field shaper's outer surface. Due to a slit in the field shaper, an induced eddy current in the field shaper's outer surface landed on the inner cylindrical surface area. The direction of current flowing through the coil, field shaper and workpiece is shown in Fig. 1. The induced eddy current in the field shaper will have equivalent frequency with a slight change in phase shift compared to the current in the coil. The eddy current flowing in the field shaper inner surface area causes another eddy current to flow in the outer surface of the tube in the opposite direction. This way, the current flowing in the field shaper inner surface and tube surface are opposite, thereby obeying Lenz's law. Therefore, strongly repelling Lorentz forces are generated between the field shaper and tube surface. The generated Lorentz force is so high that it deforms the tube radially. Since the powder is placed inside the tube with a restricted moment along the axis through the use of end plugs, therefore, as the tube squeezes radially, the powder gets compacted within very less time. Here, the field shaper acts as a current-carrying

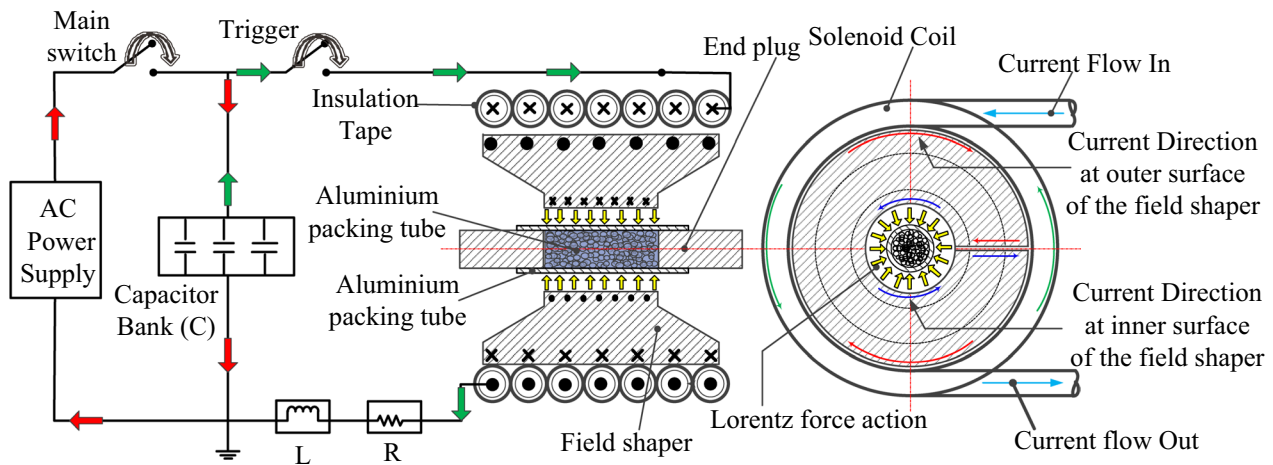


Fig. 1 Schematic diagram of the equivalent electromagnetic radial powder compaction system

conductor by coupling it to the solenoid coil inductively. It is used to increase the efficiency of the magnetic field and to uniform the distribution of the magnetic field intensity at the desired forming location [13]. The main feature of the field shaper is its “slit” portion which allows the induced eddy current to flow from the outer surface to the inner surface of the field shaper. The slit gap design must be optimized to prevent arc growth at the gap and to provide minimum magnetic pressure loss.

An action similar to electromagnetic welding, crimping, tube compression, etc., occurs at the tube’s outer surface and the field shaper during electromagnetic powder compaction. As a result, the strong Lorentz forces deform the tube and compress the powder, provided the coil and field shaper is constructed robustly. At very high discharge voltages, the magnitude of the Lorentz forces is so high and can induce the stress in the tube and powder well beyond their yield strength values within a few tens of microseconds. Since the process is very fast with significant deformation in the work-piece, it is also called the dynamic high strain rate impulse powder forming process.

2.1 Experimental Procedure

Electromagnetic radial powder compaction of pure aluminium powder experiments was conducted using a 40 kJ capacity electromagnetic forming machine. The electromagnetic forming machine parameters are: maximum discharge voltage is 20 kV, and the total capacitance is 224 μF . As shown in Fig. 2, the solenoid coil was used as conducting coil to generate the required Lorentz forces to form the powder in the tube. The coil is made of pure copper material with an 8 mm solid rod diameter. The solenoid coil used for the experiment has a mean diameter of 80 mm and a 2 mm gap maintained between each turn with the help of insulation

material. The rod is well insulated with Kapton tape to avoid sparking between the windings. The experimental workstation was arranged with a solenoid coil, copper field shaper, and Al powder sample enclosed with a packing tube (Al 6063), as shown in Fig. 3. The two terminals of the coil were connected to the high voltage capacitor bank to discharge the current. The Rogowski coil was kept between the two terminals to measure the current during experiments, and the same current curve was used for simulation. A high voltage current was imposed in the solenoid coil, producing induced currents in the field shaper and packing tube.

Generated high magnetic pressure caused the packing tube to shrink radially. As the tube shrinks inward, the powder compacts uniformly and further densify. This dynamic compaction process happened in very few microseconds. The first quarter cycle of the current curve was mainly responsible for the powder’s maximum deformation in the powder body. The maximum magnetic field between the tube and the inner surface of the field shapers achieved corresponded to the maximum current in the coil, and afterwards, there was exponential decay.

2.2 Finite Element Modelling

Ansys Maxwell 3D and Ls-Dyna software were used to simulate the modelling of the electromagnetic powder compaction process. This work adopts a loosely coupled procedure for FEM analysis of electromagnetic powder compaction. Ansys Maxwell software was used to solve the electromagnetic fields by solving Maxwell’s equation of infinite region of space with specified boundary and initial conditions. The magnetostatic solver of Ansys Maxwell was used to solve Maxwell’s equation, and it solved Maxwell’s Eqs. (1), (2), (3), and (4) [14].

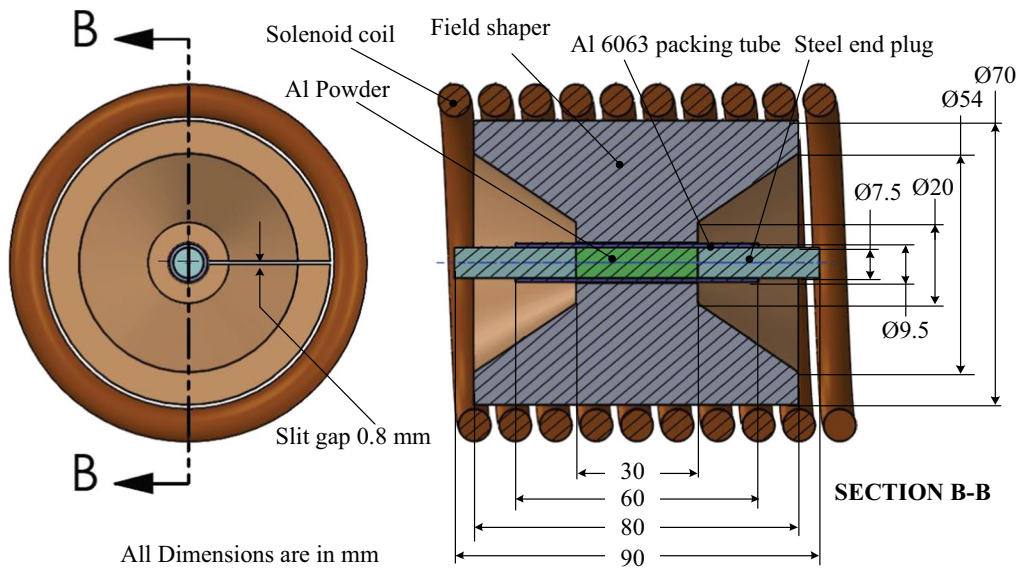


Fig. 2 Dimension of the electromagnetic radial powder compaction tool

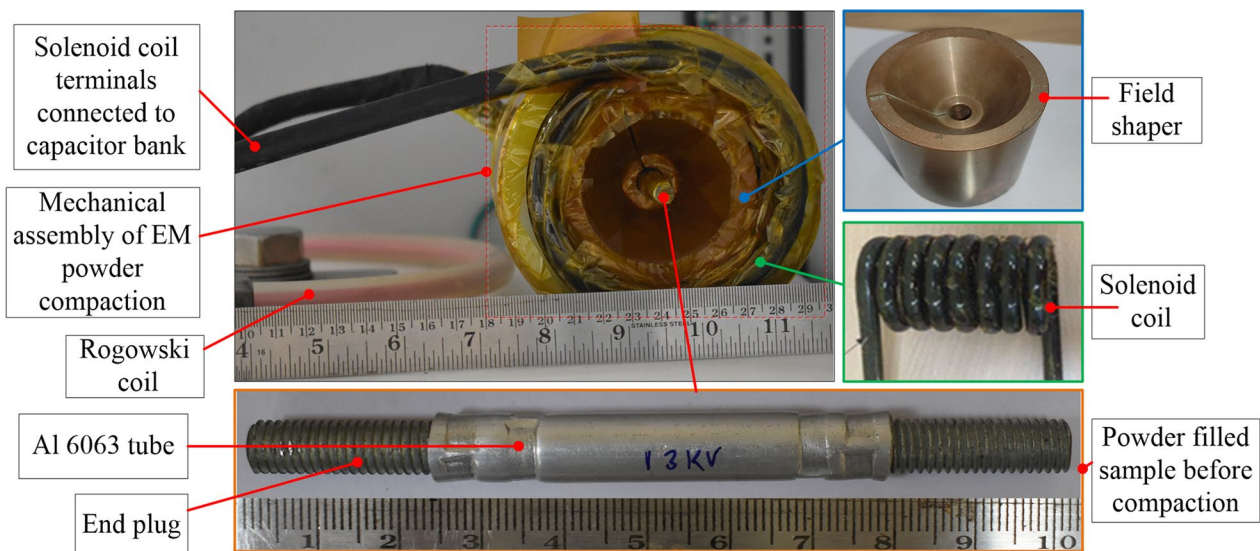


Fig. 3 Experimental set-up used for electromagnetic radial powder compaction process

$$\nabla \times H = J + \frac{\partial D}{\partial t} \quad (1)$$

$$\nabla \cdot B = 0 \quad (2)$$

$$\nabla \times E = -\frac{\partial B}{\partial t} \quad (3)$$

$$\nabla \cdot D = \rho \quad (4)$$

Ansys Maxwell eddy current solver was used to solve sinusoidal varying magnetic fields. The adaptive meshing

technique was used to achieve accuracy in the results. In this process, the magnetic pressure acting on the tube workpiece was calculated by solving the electromagnetic model using Ansys Maxwell (neglecting the tube's and powder's deformation). The pressure data was then transferred to Ls-Dyna as an input load to simulate the structural (tube and powder) deformation. This process is considered only when the structural deformations are small and abrupt changes in magnetic pressure. Although this loosely coupled method is less accurate than strongly and sequentially coupled processes, it is more flexible and can be solved quickly by simplifying the model with lower CPU costs. It is possible to estimate the

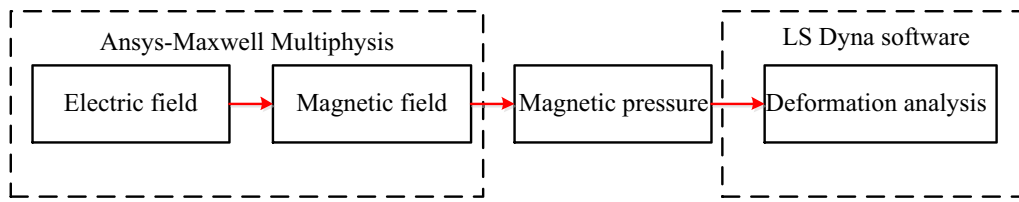


Fig. 4 Simulation process by a loosely coupled combination of ANSYS Maxwell with LS-DYNA software

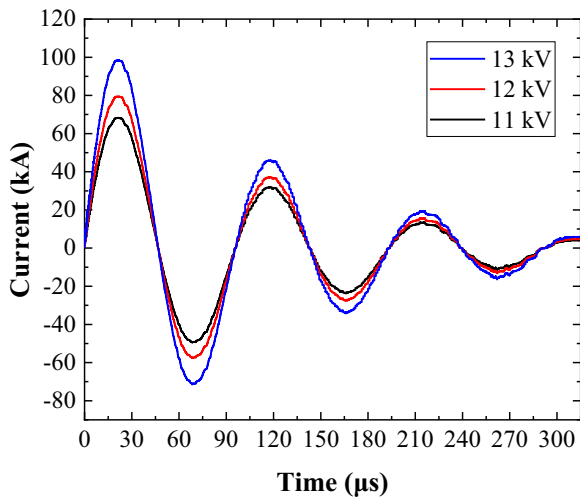


Fig. 5 Current waveform characteristics for three discharge voltages obtained in the oscilloscope

order of the charging voltage required for specific deformation of the tube and the final desirable outputs of the powder compact. The block diagram of the simulation process used for the analysis is shown in Fig. 4.

The material properties for each entity of 3D modelling for electromagnetic simulation are given in Table 1. The main load for Electromagnetic simulation is the current passing in the solenoid coil. The current waveforms captured during actual experiments are shown in Fig. 5. The same current waveforms were used as the loading. Three discharge voltage-current curves are used for the current studies in the simulation.

In the electromagnetic forming method, the current flowing in the coil is expressed by Eqs. (5) and (6),

$$I(t) = \frac{V_o}{\omega \cdot L} \times e^{-\gamma t} \times \sin(\omega \cdot t) \tag{5}$$

$$I(t) = I_{max} \times \sin(\omega \cdot t) \tag{6}$$

where V_o represents the initial charging voltage, β represents the damping coefficient (s^{-1}), ω represents the damped angular frequency (rad/s), and L represents the equivalent inductance. C represents the total capacitance of the capacitor. The equivalent inductance can be expressed by Eq. (7).

$$\text{Equivalent inductance}(L) = \frac{1}{(\omega^2 + \beta^2)C} \tag{7}$$

In electromagnetic radial powder compaction, the Lorentz force acting on the driver tube (packing tube) can be calculated as the vector product of the magnetic flux density of the field shaper and the eddy current induced in the flyer [15].

The Lorentz forces acting between the tube outer surface and field shaper are given by Eq. (8). The current density can be calculated by partially derivating the magnetic field intensity (from Maxwell’s equations) in a radial direction by Eq. (9).

$$\vec{F} = \vec{J} \times \vec{B} \tag{8}$$

$$\vec{J} = -\frac{\partial \vec{H}}{\partial r} \tag{9}$$

Therefore, the volume force acting on the driver tube can be calculated using the Eq. (10). The simplified magnetic pressure can be derived by considering the skin effect, which can be obtained using the Eq. (11).

Table 1 The mechanical properties of the materials used in the simulation [6]

Material	Relative Permeability	Bulk modulus (S/m) $\times 10^6$	Mass density (kg/m ³)	Young’s modulus (GPa)	Poisson ration
Copper	0.999910	58	8933	120	0.38
Al	1.000021	38	2689	69	0.31
Steel	–	2	7872	200	0.25

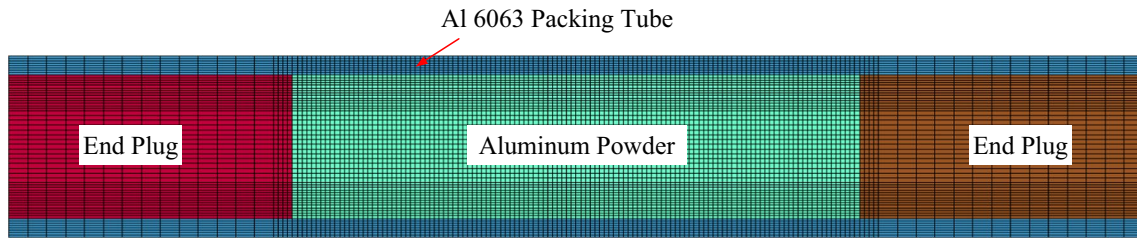


Fig. 6 Finite element model used for structural field analysis

Table 2 Geologic Cap model parameters used for aluminium powder based on ref [6, 18]

Parameter	Units	Value
Hardening law coefficient (W)	–	0.48
Hardening law exponent (D)	–	5.5e-9
Cap surface axis ratio (R)	–	2.8
Failure envelope exponent (β)	Pa ⁻¹	0
Failure envelope exponent coefficient (γ)	Pa	0
Failure envelope linear coefficient (θ)	–	0.394
Failure envelope parameter (α)	Pa	0
Initial shear modulus	GPa	13.73
Initial bulk modulus	GPa	32.74
Initial density	kg/m ³	1426

$$\vec{F} = -\frac{\partial \vec{H}}{\partial r} \vec{B} = -\frac{\partial \vec{H}}{\partial r} \mu_m \vec{H} = -\frac{1}{2} \mu_m \frac{\partial (\vec{H}^2)}{\partial r} \quad (10)$$

$$P = \int_0^t \vec{F} \partial r = \frac{1}{2} \mu_m H_{gap}^2 \quad (11)$$

where \vec{J} is current density, \vec{B} Represents magnetic field intensity, μ_m is material permeability, t is the thickness of the tube, and r is the radius of the tube. The above relationship was used to calculate the magnetic pressure manually with the help of magnetic field intensity values obtained through Ansys electromagnetic simulations. The manually calculated magnetic pressures were used as an external loading condition in Ls-Dyna on the outer surface of the tube material. The FEM structural meshed model is shown in Fig. 6. It was assumed that steel end plugs were modelled as a rigid material model, and it is constrained in all degrees of freedom during simulation. The powder was assumed to be a continuous compressible material, and the MAT_GEOLOGIC_CAP_MODEL keyword [16] was used to model the powder

for predicting its behaviour during the compaction process. The model constants of the GEOLOGIC_CAP_MODEL for aluminium material are shown in Table 2. The packing tube is modelled using the MAT_JOHNSON_COOK keyword [16] material model. The Johnson-Cook constitutive equation was used to study the behaviour of the tube during compression. The Johnson-Cook strength equation [17] considers the effect of plastic strain and plastic strain rate in the high rate forming process, which can be expressed by Eq. (12). The model constants for the Al 6063 packing tube are given in Table 3.

$$\sigma = (A + B\epsilon^n) \left(1 + C \ln \left(\frac{\dot{\epsilon}}{\dot{\epsilon}_0} \right) \right) \left(1 - \left(\frac{T - T_{room}}{T_m - T_{room}} \right)^n \right) \quad (12)$$

The combined effect of strain hardening, strain rate and thermal softening was taken care of by the Johnson-Cook model constants A, B, C and n, respectively. Where σ represents the equivalent plastic stress (MPa), ϵ represents the equivalent plastic strain, $\dot{\epsilon}$ represents the equivalent plastic strain rate (s⁻¹), $\dot{\epsilon}_0$ = reference strain rate, and m and n are material constants.

Johnson Cook’s material model has been considered for describing the tube deformation since the material model is well suited for high strain rate forming processes such as electro hydroforming, electromagnetic forming, and explosion forming process.

2.3 Process Input Characteristics

In electromagnetic powder compaction, the current is an important parameter taken from the Rogowski coil experiment. The current waveforms at various discharge voltages are shown in Fig. 5. The first half of the cycle curve is given as input current to analyze the electromagnetic phenomena in the Ansys Maxwell to obtain the magnetic

Table 3 Values of Johnson-Cook material constant for Aluminium 6063 packing tube [19]

Elastic modulus	Poisson’s ratio	Density	A (MPa)	B (MPa)	C	n
69.0 GPa	0.320	2700 kg/m ³	176.40	63.90	0.0036	0.07

field intensity. The results are only discussed for the first period of the current input curve [20].

3 Results and Discussions

In this work, only the first half of the current wave is considered for the numerical study of electromagnetic powder compaction in Ansys Maxwell and Ls-Dyna structural analysis. The magnetic pressure developed during the first half of the cycle is considered responsible for the plastic deformation of the tube and powder. The current is applied in the increment of 2 μs throughout transient magnetic field analysis. Since it is a loosely coupled FEM analysis, the effect of deformation of the workpiece on the evolution of the Lorentz forces is disregarded in the present work. Above mentioned assumptions are acceptable only when the deformations are moderate. However, experimental validations are still required.

The structural analysis is carried out on the tube and powder body in Ls-Dyna separately; the cross-sectional view of the model used for further investigation is shown in Fig. 6. The averaged magnetic field pressure is used as an external loading condition in the FEM analysis of the structural deformation. The pressure acts on the outer tube surface as an external loading boundary condition over 30 mm working length. The structural finite element model has 127,000 elements in the powder body, 19,170 elements in the end plug, and the tube has 74,880 elements. All the structural parts have meshed with eight-node quad elements in the Ls-Dyna analysis. The Coulomb friction constant value of 0.25 is applied between all the contacting surfaces [6].

3.1 Magnetic Field and Pressure Distribution Analysis

The maximum current was achieved at 22 μs which can be observed from the current waveforms obtained in the oscilloscope shown in Fig. 5. The magnetic flux density variation with time is shown in Fig. 7a. As expected, the magnetic field intensity was following the current input trend. The maximum magnetic field was achieved at around 22.4 T at 22 μs, corresponding to the input voltage of 13 kV. The magnetic field intensity was found to increase with input discharge voltage.

Figure 7b represent the variation of magnetic field intensity at various location in the Electromagnetic powder compaction tool. It was observed that maximum magnetic field intensity is located in the space between the inner surface of the field shaper and the outer surface of the packing tube. As expected, the field shaper enhanced the magnetic field intensity by more than two times. At the interface of the field shaper and coil, the magnetic field intensity was about 10.5 T, whereas, at the interface of the tube and field shaper, the magnetic field intensity (B) was 22.4 T. Therefore, the results were in good agreement, so the finite element analysis model is valid from the field shaper’s working point of view. The magnetic pressure is calculated using the empirical relationship given in Eq. (11) from the magnetic field values over the simulation time. As expected, the magnetic pressure varied parabolically with magnetic field intensity. The magnetic pressure obtained was 200 MPa, corresponding to 13 kV voltage, reaching its maximum value at 22 μs as the current reached its maximum value. The variation in the magnetic pressure with time at three different values of the discharge voltages is shown in Fig. 8a and b shows the variation in magnetic field intensity at different depths of the

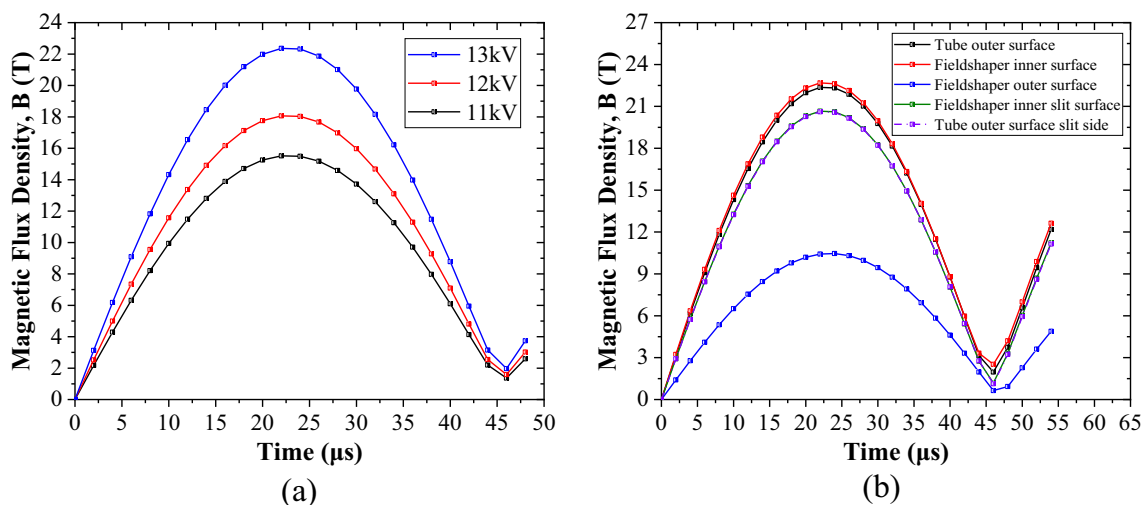


Fig. 7 Variation of the magnetic field with time at a three voltage discharges in the conductors and b at different locations

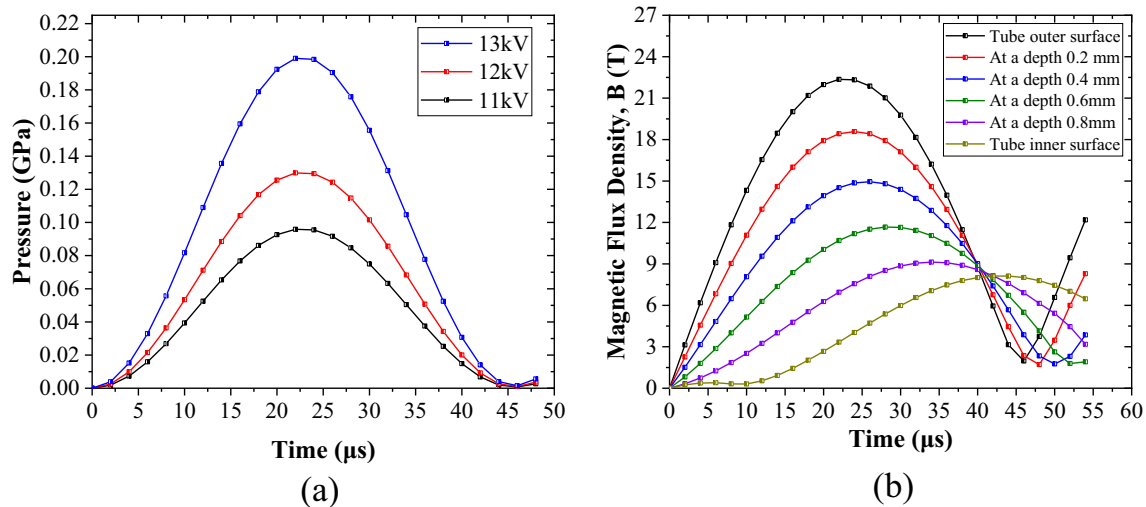


Fig. 8 Variation in the magnetic pressure with time for various discharge voltages

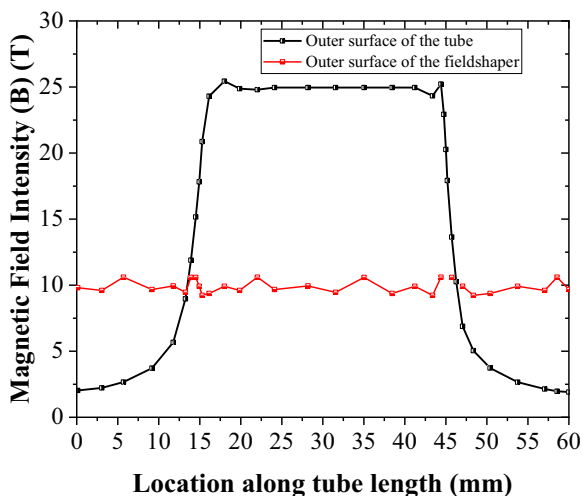


Fig. 9 Variation of Magnetic field distribution along the length at 13 kV after discharge for 22 μs

packing tube over time. It can be observed that the magnetic flux intensity at the outer surface of the tube is decaying at a faster rate compared to the other location. The magnetic flux intensity was observed to be decreasing from the outer surface to the inner surface.

The magnetic flux density gradually started increasing from the packing tube's outer surface to the packing tube's inner surface after the current discharge elapsed time reached 40 μs. Figure 9 shows the varying magnetic field intensity along the length of the workpiece. It was calculated over a length of 60 mm, which is equivalent to the packing tube length. The magnetic field density was observed to be more uniform and maximum at the inner step of the field shaper. Therefore, the magnetic pressure

developed on the workpiece tube was uniformly distributed in the axial direction. The magnetic flux was abruptly reduced, resulting from moving away from the step zone of the field shaper. However, the magnetic field was not uniform on the circumference of the workpiece tube. Figure 9 shows that magnetic field intensity decreased at the slit location, slightly lower than in other locations. Due to a slit gap in the field shaper, there was a minor loss in the magnetic field, which can be minimized by maintaining the optimum slit gap.

3.2 Analysis of Powder Deformation During Compaction

The finite element analysis investigated the tube and powder deformation at various time steps. Figure 10 represents the deformation of the powder and tube at 13 kV discharge voltage magnetic pressure. It can be observed the maximum deformation is achieved at 22 μs which corresponds to the maximum current flowing in the coil. During the electromagnetic powder compaction process, the porosity of the aluminium powder reduced while the density and strength of the powder compact sample increased. Based on the deformed geometry and loading used in the simulation, it can be observed that the changes to the porosity are non-uniform along the radius line from the outer surface to the axis of the powder compact. Compared to the compact axis portions of the powder, the metal powder in the upper layer portion (just beneath the inner tube surface) was found to be more compact. Along the sample axis, the powder was compacted less because of frictional resistance and the pressure wave strength was insufficient to transfer the momentum.

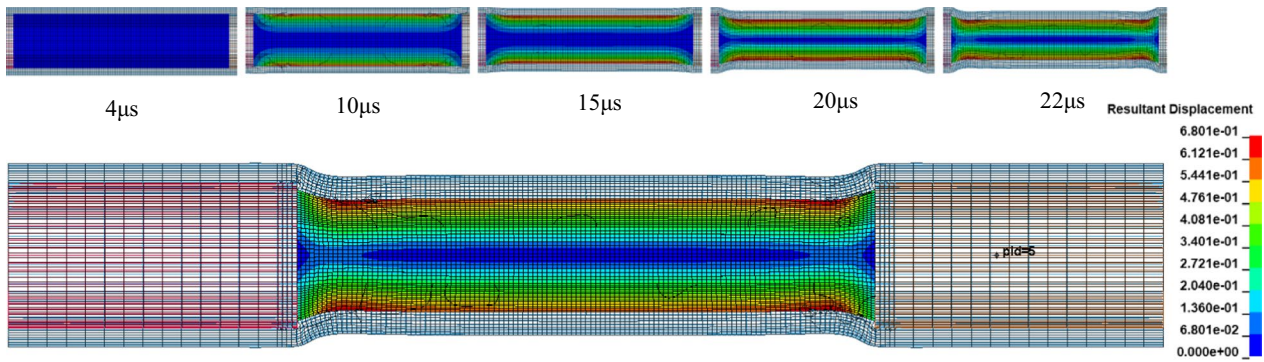


Fig. 10 Relative deformation distribution in the powder and tube at different time steps

3.3 Comparison of Experimental and Simulation Results

The simulation and experimental results were validated using the final compact diameter with the deformed packing tube. Figure 11a and b represent the final deformed sample in simulation and experimental, respectively, at 13 kV discharge voltage. The final diameter values of the simulation were in good agreement with the experimental results. The error between the simulation and experimental results in predicting the final shape and size of the sample was not exceeding 5%. The comparison between experimental and simulation results at different discharge energies is plotted in Fig. 12a. The variation in the displacement with time at three different values of the discharge voltages is shown in Fig. 12b.

3.4 Effective (v-m) Stress Analysis of the Powder body

Figure 13 shows the contour plot of the Von-Mises stress in the powder compacted sample prepared at various compaction voltages. The results indicated that the stresses were high in the centre when the powder compacted at higher compaction voltages. The stresses were at the surface when the powder compacted at lower energies. Distributions of effective stress (v-m stress) inside the aluminium compact sample throughout the whole process were numerically predicted, and the maximum stress was found to be 300 MPa at the centre of the powder compaction, as shown in Fig. 13c when the powder got compacted at 13 kV discharge voltage.

3.5 Resultant Velocity Analysis

Figure 14 shows the variation of impact velocity of the packing tube to the powder outer layer at different discharge voltages. During electromagnetic radial powder compaction of Al powder cylindrical compound

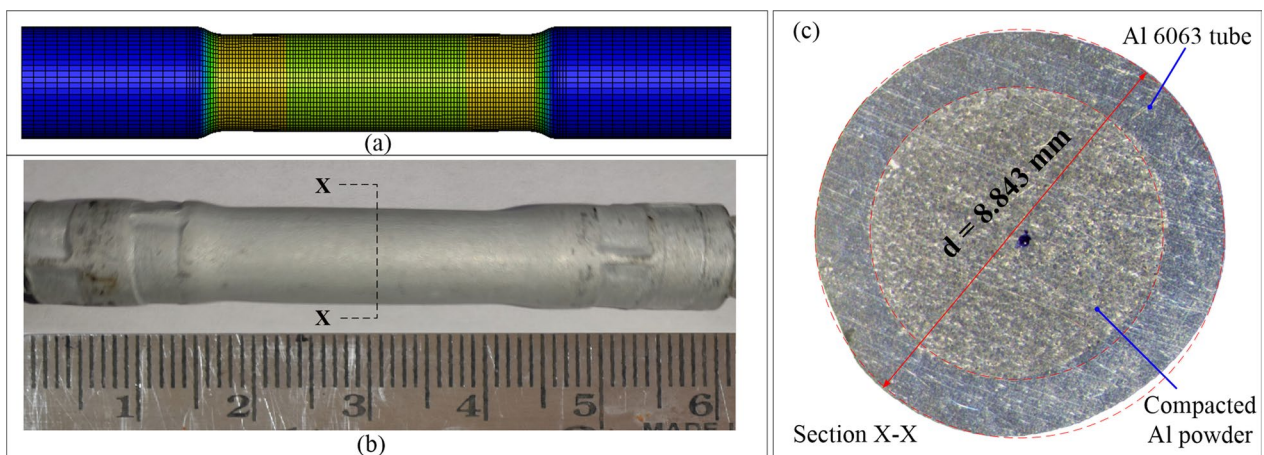


Fig. 11 Deformation analysis between experimental and simulation result at 13 kV compaction voltage

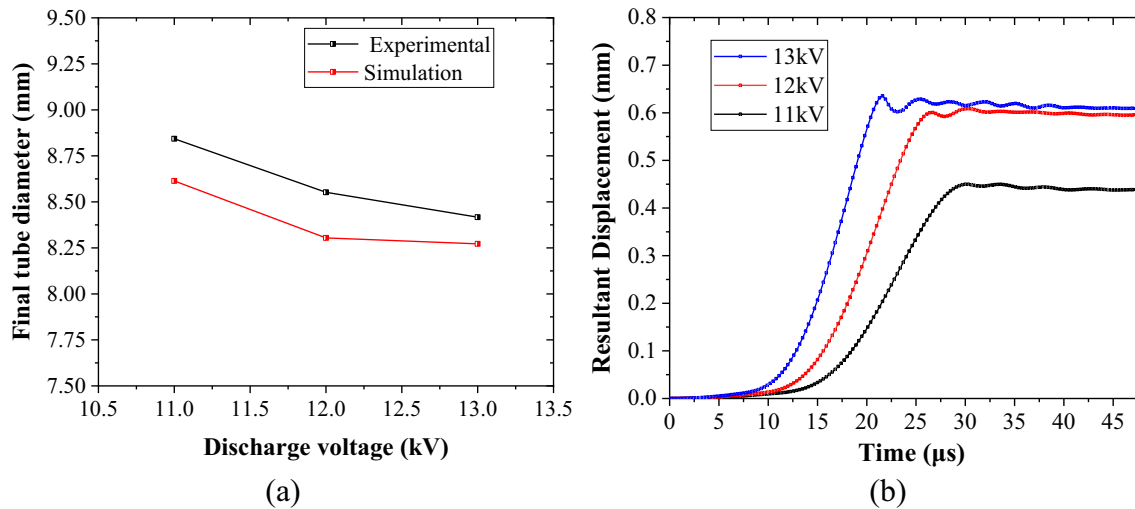


Fig. 12 Experimental and simulation results compared with a final diameter of the compacted sample with packing tube at a various discharge voltage

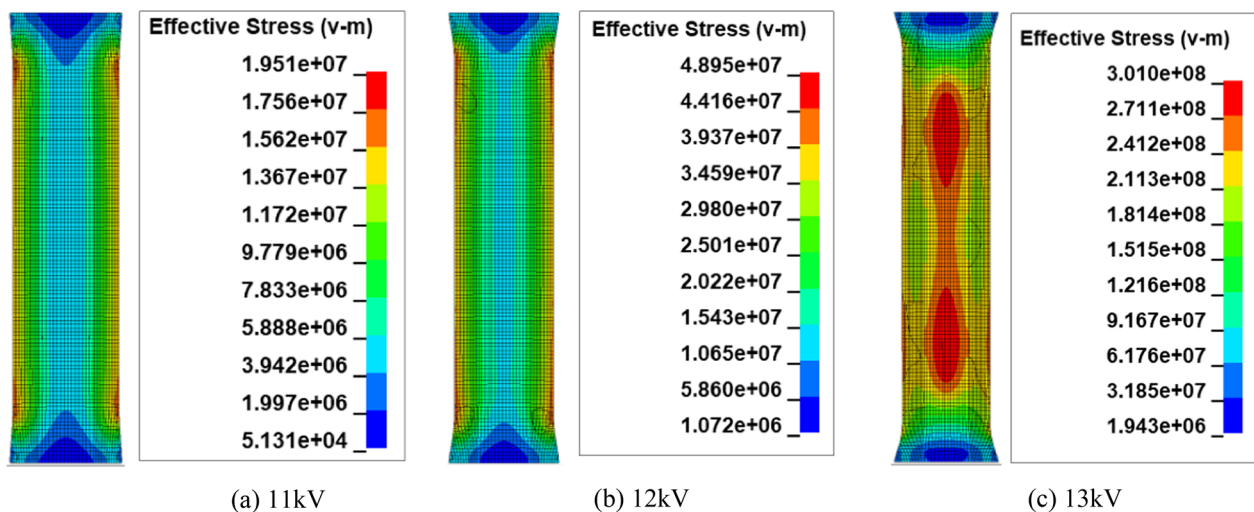


Fig. 13 Variation of effective (v-m) stress distribution in the powder compact at a various input discharge voltage

preparation, with discharge voltage of 13 kV, maximum compaction pressure reached 0.2 MPa, with the highest velocity being approximately 80 m/s.

The resultant velocity plot shows that the tube initially accelerates to a maximum velocity of 80 m/s within 17.5 μ s of time, then slowly decelerates, corresponding to a 13 kV discharge voltage. The velocity distribution of the tube gives information about the momentum transfer to the powder from the tube for its compaction. The variation also helps identify the particle's speed during the compaction process.

4 Conclusions

A Geologic cap model was used to describe the powder compaction process resulting from electromagnetic Lorentz forces. Loosely coupled structural analysis is carried out in the Ls-Dyna explicit. Electromagnetic pressure was calculated using Ansys Maxwell multi-physics software and is used as a boundary loading condition for powder compaction. The important findings of this work are as follows:

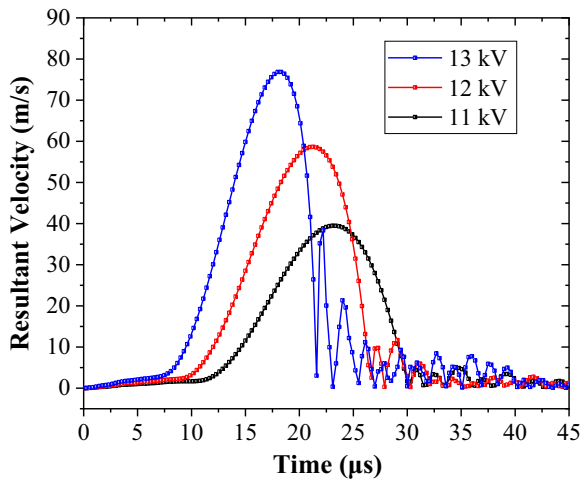


Fig. 14 The variation of resultant velocity of the tube at various discharge voltages

- The magnetic field variation with various discharge voltages and the effect of field shaper on magnetic field density distribution analysis was carried out from the results of Ansys Maxwell. Using a field shaper in electromagnetic powder compaction resulted in a concentrated magnetic field. Thereby, it enhanced the Lorentz forces significantly.
- The slit in the field shaper caused the slightly uneven distribution of the magnetic field intensity on the circumference of the powder compacting sample, resulting in uneven distribution of the deformation of the compacted body and its density.
- Experimental results were compared with simulation results, and it was found that the results are in good agreement with 95%. Hence simulations were proven to be valid for predicting the deformation, stresses and impact velocity.
- The final diameters of the compacted samples were taken for comparison from the experimental and simulation results. Von-Mises stress distribution results can also be used to predict the stress levels in compacted samples.
- The impact velocity of the driver tube was maximum and reached 80 m/s when the compaction discharge was 13 kV.

Acknowledgements The author would like to thank the Indian Institute of Technology, Goa, for allowing using its facility to complete this research work.

Author contributions All authors read and approved the final manuscript.

Funding Not applicable.

Availability of data and materials Not applicable.

Declarations

Competing interests The author declares that they have no conflict of interest.

References

1. Psyk, V., Risch, D., Kinsey, B. L., Tekkaya, A. E., & Kleiner, M. (2011). Electromagnetic forming—A review. *Journal of Materials Processing Technology*, *211*, 787–829. <https://doi.org/10.1016/j.jmatprotec.2010.12.012>
2. Boltachev, G. S., Chingina, E. A., Spirin, A. V., & Volkov, N. B. (2019). Densification rate influence on nanopowder compactibility. *Mater Phys Mech*, *42*, 165–177. https://doi.org/10.18720/MPM.4222019_2.
3. Yan, S., Lei, Y., Huang, S., Wang, Q., Zhou, M., Hu, J., & Zou, F. (2019). Dynamic analysis of electromagnetic compaction of Ag-Cu-Sn multivariate mixed metal powders for brazing. *International Journal of Applied Electromagnetics and Mechanics*, *60*, 457–476. <https://doi.org/10.3233/JAE-180021>
4. Mamalis, A. G., Vottea, I. N., & Manolakos, D. E. (2002). Fabrication of metal/sheathed high-Tc superconducting composites by explosive compaction/cladding: Numerical simulation. *Materials Science & Engineering. B, Solid-State Materials For Advanced Technology*, *90*, 254–260. [https://doi.org/10.1016/S0921-5107\(01\)00913-8](https://doi.org/10.1016/S0921-5107(01)00913-8).
5. Han, L. H., Elliott, J. A., Bentham, A. C., Mills, A., Amidon, G. E., & Hancock, B. C. (2008). A modified Drucker-Prager Cap model for die compaction simulation of pharmaceutical powders. *International Journal Of Solids And Structures*, *45*, 3088–3106. <https://doi.org/10.1016/j.ijsolstr.2008.01.024>.
6. Selig, S. G., & Doman, D. A. (2015). Finite element simulation of the compaction and springback of Alumix 321 PM alloy. *Journal of Applied Mathematics*. <https://doi.org/10.1155/2015/283843>
7. Akhmetshin, L. R., Smolin, I. Y., & Buyakova, S. P. (2021). Numerical study of hard-metal powder compaction. *IOP Conference Series: Materials Science and Engineering*, *1093*, 012002. <https://doi.org/10.1088/1757-899x/1093/1/012002>.
8. Chtourou, H., Guillot, M., & Gakwaya, A. (2002). Modeling of the metal powder compaction process using the cap model. Part I. Experimental material characterization and validation. *International Journal of Solids And Structures*, *39*, 1059–1075. [https://doi.org/10.1016/S0020-7683\(01\)00255-4](https://doi.org/10.1016/S0020-7683(01)00255-4).
9. Ni, P., Liu, H., Dong, Z., Ma, Y., & Wang, X. (2022). Laser shock dynamic compaction of aluminum powder. *Journal Of Manufacturing Processes*, *77*, 694–707. <https://doi.org/10.1016/j.jmapro.2022.03.056>.
10. Babaei, H., Mostofi, T. M., Alitavoli, M., Namazi, N., & Rahmanpoor, A. (2016). Dynamic compaction of cold die aluminum powders. *Geomech Eng*, *10*, 109–124. <https://doi.org/10.12989/gae.2016.10.1.109>.
11. Olevsy, E. A., & Dudina, D. V. (2018). Magnetic pulse compaction. *Field-assisted sintering*. Springer. https://doi.org/10.1007/978-3-319-76032-2_9.
12. Kim, D., Park, K., Kim, K., Cho, S., & Hirayama, Y. (2019). Cold Compaction behavior of nano and micro aluminum powder under high pressure. *Compos Res*, *32*, 141–147.
13. Dond, S. K., Kulkarni, M. R., Kumar, S., Saroj, P. C., & Sharma, A. (2015). Magnetic field enhancement using field shaper for Electromagnetic welding system. In *2015 IEEE applied electromagnetics conference (AEMC) 2016* (pp. 12–13). <https://doi.org/10.1109/AEMC.2015.7509219>.
14. Inc., A. (2010). Maxwell 3D User's Guide. *15*, 92–101.

15. Stankevic, V., Lueg-Altho, J., Hahn, M., Tekkaya, A. E., Zurauskienė, N., Dilys, J., Klimantavicius, J., Kersulis, S., Simkevicius, C., & Balevicius, S. (2020). Magnetic field measurements during magnetic pulse welding using cmr-b-scalar sensors. *Sensors (Switzerland)*, *20*, 1–14. <https://doi.org/10.3390/s20205925>.
16. Livermore Software Technology Corporation (2014). LS-DYNA Keyword User's Manual Volume II R7.1.
17. Johnson, G. R., & Cook, W. H. (1983). A computational constitutive model and data for metals subjected to large strain, high strain rates and high pressures. In *Seventh international symposium on ballistics* (pp. 541–547).
18. Lee, S. C., & Kim, K. T. (2002). Densification behavior of aluminum alloy powder under cold compaction. *International Journal of Mechanical Sciences*, *44*, 1295–1308. [https://doi.org/10.1016/S0020-7403\(02\)00054-1](https://doi.org/10.1016/S0020-7403(02)00054-1)
19. Cai, D., Liang, J., Ou, H., Li, G., & Cui, J. (2021). Mechanical properties and joining mechanism of electrohydraulic expansion joints for 6063 aluminum alloy/304 stainless steel thin-walled pipes. *Thin-Walled Structure*, *161*, 107427.
20. Haiping, Y., & Chunfeng, L. (2008). Effects of current frequency on electromagnetic tube compression. *Journal of Materials Processing Technology*, *9*, 1053–1059. <https://doi.org/10.1016/j.jmatp.rotec.2008.03.011>

Publisher's Note Springer Nature remains neutral with regard to jurisdictional claims in published maps and institutional affiliations.

Springer Nature or its licensor (e.g. a society or other partner) holds exclusive rights to this article under a publishing agreement with the author(s) or other rightsholder(s); author self-archiving of the accepted manuscript version of this article is solely governed by the terms of such publishing agreement and applicable law.



Nadimetla Thirupathi is a PhD student in the School of Mechanical Sciences, Indian Institute of Technology Goa, India. He received his M. Tech degree in Production Engineering from the University College of Engineering, Osmania University, Hyderabad, Telangana, India. His main research interests include electromagnetics powder forming, and welding.



Ramesh Kumar is an Assistant Professor in the Department of Mechanical Engineering at Saharsa College of Engineering, Saharsa, Bihar, India. He received his PhD degree from the Indian Institute of Technology Guwahati, India. He has published several papers in peer-reviewed journals and international conferences in electromagnetics manufacturing. His main research interests include electromagnetics manufacturing.



Sachin D. Kore is a Professor in the School of Mechanical Sciences at the Indian Institute of Technology Goa, India. He received his PhD degree from the Indian Institute of Technology Bombay, India, and he was a Postdoctoral Fellow of CAMJ, University of Waterloo, Canada. He has published several papers in peer-reviewed journals and international conferences in the field of electromagnetics manufacturing and solid-state welding. His areas of interest are electromagnetic: welding, perforation, crimping and powder compaction, Wire Arc additive manufacturing, and Friction stir welding.

His areas of interest are electromagnetic: welding, perforation, crimping and powder compaction, Wire Arc additive manufacturing, and Friction stir welding.